

# Formation and Stabilization of Ground and Excited State Singlet O<sub>2</sub> upon Recombination of <sup>3</sup>P Oxygen on Amorphous Solid Water

Marco Pezzella, Debasish Koner and Markus Meuwly\*

*Department of Chemistry, University of Basel, Klingelbergstrasse 80, CH-4056 Basel,  
Switzerland.*

E-mail: m.meuwly@unibas.ch

### Abstract

The recombination dynamics of  $^3\text{P}$  oxygen atoms on cold amorphous solid water to form triplet and singlet molecular oxygen ( $\text{O}_2$ ) is followed under conditions representative for cold clouds. It is found that both, formation of ground state ( $X^3\Sigma_g^-$ )  $\text{O}_2$  and molecular oxygen in the two lowest singlet states ( $a^1\Delta_g$  and  $b^1\Sigma_g^+$ ) is possible and that the species can stabilize. The relative proportions of the species is approximately 1:1:1. These results also agree qualitatively with a kinetic model based on simplified wavepacket simulations. As the chemical reactivity of triplet and singlet  $\text{O}_2$  is different it is likely that substantial amounts of  $a^1\Delta_g$  and  $b^1\Sigma_g^+$  oxygen influences the chemical evolution of cold clouds.

## 1 Introduction

The role of electronically excited states of oxygen, in particular that of singlet  $\text{O}_2$ , is well established in biological, atmospheric<sup>18,27</sup> and combustion chemistry.<sup>8,9,28</sup> Combustion processes involving  $\text{H}_2$ ,  $\text{CO}$  or  $\text{CH}_4$  are accelerated in the presence of  $\text{O}_2$  in its  $a^1\Delta_g$  and  $b^1\Sigma_g^+$  states, compared to reactions with  $\text{O}_2$  in its  $X^3\Sigma_g^-$  ground state.<sup>28</sup> No such effects are observed for the combustion of  $\text{N}_2$ .<sup>28</sup> Computational studies<sup>18</sup> on  $\text{CH}_2 + \text{O}_2$  and thiophene<sup>27</sup> probe different aspects of  $\text{O}_2$  excited state reactivity: in the first case no difference between the ground state and the second excited state is encountered, while for thiophene the singlet oxygen channel seems to be dominant.

Recently, the possibility of oxygen diffusion<sup>25</sup> and recombination of two  $^3\text{P}$  oxygen to form ground state  $\text{O}_2$  in dark molecular clouds was established.<sup>24</sup> Given this, it is also of interest to explore the possibility that molecular oxygen can be formed in low lying electronically excited states under interstellar conditions. Experimental spectroscopic observations show

that recombination of two oxygen atoms ( $^3P$ ) generated from photolysis of  $^{16}\text{O}_2$  using far-ultraviolet light in neon matrices at low temperature ( $T \sim 5$  K) leads to formation of  $\text{O}_2$  in its  $X^3\Sigma_g^-$ ,  $a^1\Delta_g$ ,  $b^1\Sigma_g^+$ , and additional, more highly excited electronic states<sup>7</sup> although the relative populations of the states were not reported. The first ( $^1\Delta_g$ ) and second ( $^1\Sigma_g^+$ ) excited states are of particular interest, due to their higher reactivity compared to the ground state. In the gas phase and in isolation the two transitions  $a^1\Delta_g \rightarrow X^3\Sigma_g^-$  and  $b^1\Sigma_g^+ \rightarrow X^3\Sigma_g^-$  are symmetry forbidden with radiative lifetimes of 4000 and 150 s, induced by magnetic-dipole and electric-quadrupole interactions,<sup>12</sup> respectively. A major contributor to the  $b^1\Sigma_g^+ \rightarrow X^3\Sigma_g^-$  transition is the first order Spin-Orbit coupling close to the ( $\nu = 28, N = 5$ ) of the ground state.<sup>17</sup> Collision induced emission has been reported to accelerate the  $a^1\Delta_g \rightarrow X^3\Sigma_g^-$  transition, being 9 orders of magnitude faster (500  $\mu\text{s}$  vs. 4000 s) than the radiative emission.<sup>15</sup> However, in the presence of an environment, these transitions can occur due to the perturbations induced by the environment. Relaxation from the  $^1\Sigma_g^+$  state to  $^3\Sigma_g^-$  occurs *via* Inter System Crossing (ISC), governed by Spin Orbit Coupling (SOC) that can be described using the Landau Zener (LZ) formalism.<sup>10,19</sup>

Here, the possibility is explored that upon  $\text{O}(^3P) + \text{O}(^3P)$  recombination on Amorphous Solid Water (ASW) not only the ground ( $X^3\Sigma_g^-$ ), but also electronically excited states of molecular oxygen, i.e.  $\text{O}_2$  ( $b^1\Delta_g$  and  $a^1\Sigma_g^+$ ) are formed, stabilized and populated. ASW, which is a form of glassy water, is considered to be the main component of ices on top of the small grains present in interstellar clouds.<sup>1,4</sup> The high porosity of ASW<sup>2,3,5</sup> makes it a good catalyst for gas-surface reactions involving oxygen,<sup>6,11,16,24? -26</sup> hydrogen,<sup>14</sup> carbonaceous<sup>21?</sup> and nitrogen-containing<sup>20</sup> species and helps maintaining those species on the surface.<sup>22?</sup> Using reactive molecular dynamics simulations<sup>29</sup> with nonadiabatic transitions the dynamics, relaxation and population distribution after partial vibrational equilibration of  $\text{O}_2$  in the three lowest electronic states is characterized in the following.

## 2 Results

In the following, a two- and a three-state model is explored. The two-state model provides an overview of the expected dynamics for an electronic transition which becomes allowed in the presence of an environment. For the more complete three-state model only two out of the three transitions occur.

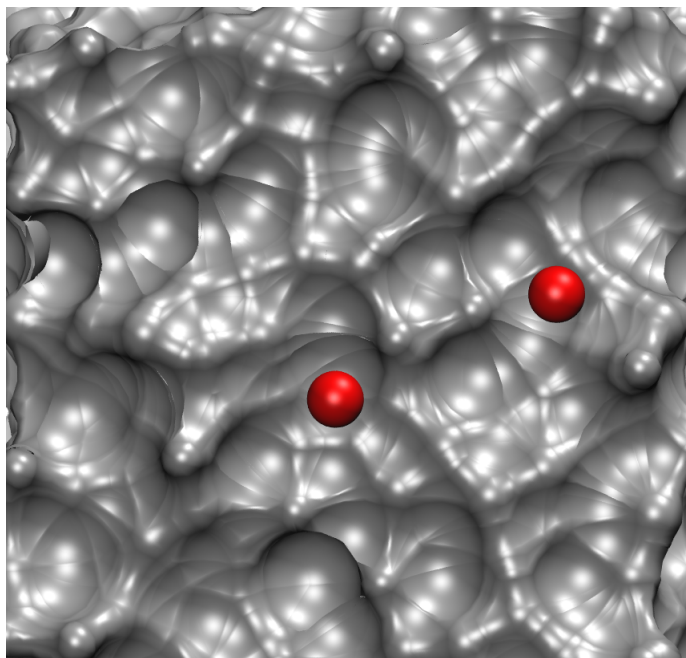


Figure 1: The simulation system with water bulk represented in grey, with the two oxygen atoms on top of the surface in red.

### 2.1 Two state model

First, a two state model involving the  $X^3\Sigma_g^-$  and  $b^1\Sigma_g^+$  states is considered. For this, different types of simulations were carried out: a) 2 ns simulations with both oxygen atoms inside bulk ASW; b) five 8 ns simulations with the two oxygen atoms on the surface and rebinding into the  $^3\Sigma_g^-$  state initially; c) 2200 simulations run for 400 ps on the surface (1100 recombining into the  $^3\Sigma_g^-$  state and 1100 into the  $^1\Sigma_g^+$  state).

For the analysis two quantities are considered: the time between two consecutive transitions  $\tau_c$  and the total crossing time from the first to the last transition,  $\tau_{LZ}$ . Per definition, after  $\tau_{LZ}$  no further transitions between the states are observed.

For simulations inside ASW bulk (see Figure S2),  $O_2$  is formed in its  $b^1\Sigma_g^+$  state after  $\sim 750$  ps and stabilized after two scattering events at 103.5 and 670 ps (see Figure S2), with  $\tau_{LZ} = 30$  ps. This time interval is characterized by the abrupt change in the kinetic energy by  $\sim 40$  kcal/mol due to the difference in potential energy between the two states, see Figure S1. After this time no further transitions are encountered during the simulation and the molecule vibrationally relaxes and is stabilized in the  $b^1\Sigma_g^+$  state.

Results for a simulation on the ASW surface are shown in Figure 2. Starting from an initial separation of  $4.8 \text{ \AA}$ , recombination occurs after 20 ps with the molecule forming in the  $b^1\Sigma_g^+$  state followed by an extended time ( $\tau_{LZ} = 70$  ps) during which crossings between the two states occur with final relaxation in the  $b^1\Sigma_g^+$  state. The identity of the state is followed explicitly in the simulations. This also allows to trace the kinetic energy of the  $O_2$  molecule during the time it samples one or the other state, see green and black traces in Figure 2.

Five simulations were run by rebinding into the  $b^1\Sigma_g^+$  state for a total of 8 ns to determine whether further transitions are observed after the molecule relaxes below the crossing point after  $\tau_{LZ}$ . Three trajectories lead to bound  $O_2$ : one in the  $X^3\Sigma_g^-$  and the other two in the  $b^1\Sigma_g^+$  state and transitions occur with a sharp distribution peaked at the crossing point ( $2.209 \text{ \AA}$ ). In the other two simulations the two atoms do not recombine within 8 ns but rather continue to sample an unbound state. The time interval between the first and last transition (i.e.  $\tau_{LZ}$ ) and between two single transitions (i.e.  $\tau_c$ ) is consistent with results in Figure S4 discussed further below. The time series of two of those simulations are reported in Figure S3.

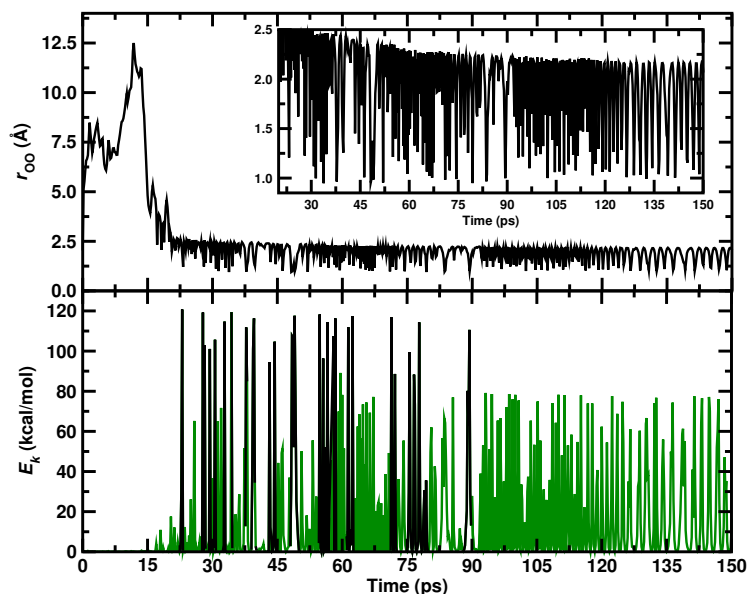


Figure 2: Top: time evolution of the interatomic distance between two oxygen atoms on top of ASW. Recombination occurs after 16 ps. Bottom: kinetic energy for  $O_2$  system during 150 ps. Formation of the bound state is reflected by the sharp increase of the kinetic energy of the two oxygen atoms at 16 ps. Transitions between the  $X^3\Sigma_g^-$  (black)  $b^1\Sigma_g^+$  (green) are observed between 17 and 100 ps. After this the system localizes on the  $b^1\Sigma_g^+$  state. The average over the green and black traces also reflects the different binding energy (38.7 kcal/mol) for the two electronic states, see Figure S1.

Next, the results from the 2200 rebinding simulations on the surface are analysed. Initially, the two O atoms are separated by  $6.07 \pm 2.13 \text{ \AA}$ . For  $\sim 80 \%$  of the simulations  $\text{O}_2$  is formed, consistent with previous work.<sup>25</sup> Half of these simulations initially recombine into the  $X^3\Sigma_g^-$  state and the other half into  $b^1\Sigma_g^+$ . The average time interval between two consecutive transitions ( $\langle\tau_c\rangle$ ) is  $47.4 \pm 11.7 \text{ fs}$ , for an average number of  $1224 \pm 537$  transitions per trajectory, independent of the initial state into which rebinding takes place. The distribution  $p(\tau_c)$  is shown in Figure S4. On average, one crossing every two vibrational periods is observed before sufficient vibrational energy has been dissipated and the crossing point can not be reached anymore energetically. After this, vibrational relaxation on the final electronic state takes place on considerably longer time scales.

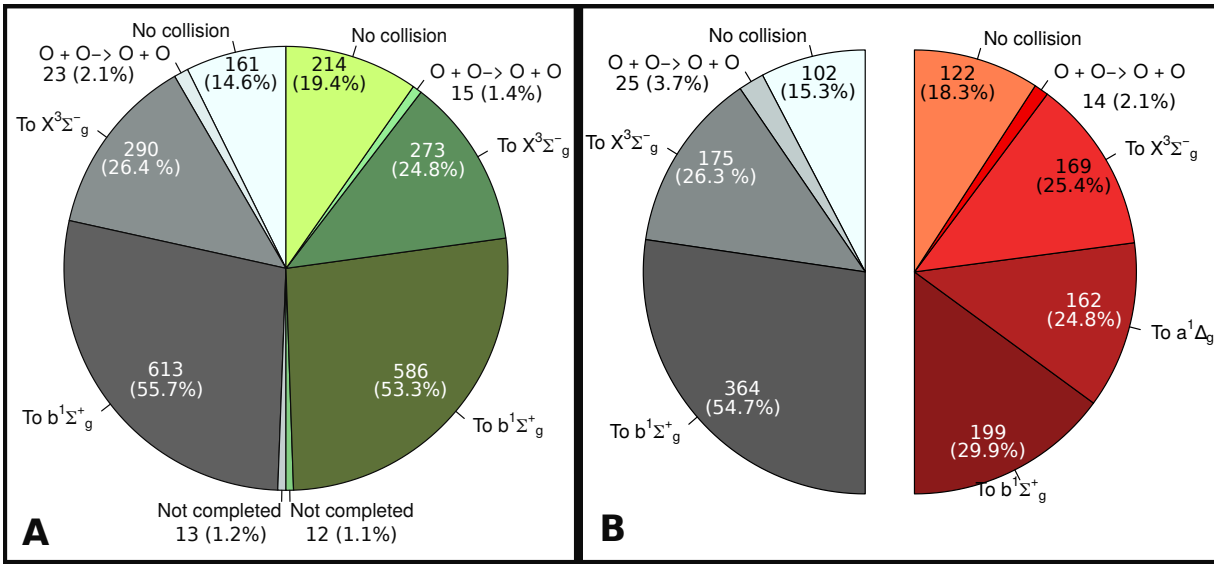


Figure 3: Panel A: Classification of outcome of the simulations, in black those rebinding into the  $X^3\Sigma_g^-$  state and in green those initially rebinding into the  $b^1\Sigma_g^+$  state. Within 400 ps, 82.1% of them lead to the  $\text{O}_2$  recombination. In both sets, the majority of simulations leads to the  $b^1\Sigma_g^+$ , while  $\sim \frac{1}{3}$  reaches the ground state. Panel B: comparison between the two state model (left, grey) and the three-state model (right, red). For the two-state model, 666 random simulations from the two states models were sampled. The population of the  $X^3\Sigma_g^-$  is similar for the two models whereas the population of the  $b^1\Sigma_g^+$  state from the two-state model splits into two similar fractions for the three-state model which includes two excited states,  $b^1\Sigma_g^+$  and  $a^1\Delta_g$ . The remaining channels are similarly populated.

Out of the 1100 trajectories which recombine into one of the two electronic states, 903 and

859 simulations localize either in  $X^3\Sigma_g^-$  or  $b^1\Sigma_g^+$ , see Figure 3. Following this, O<sub>2</sub> vibrational relaxation takes place on considerably longer time scales. The distribution of O–O separations  $r$  at which changes in the electronic state occur is shown in Figure S5A. From all 2200 trajectories,  $\sim 66\%$  (1756 trajectories) recombine into the  $^1\Sigma_g^+$  state while 33% lead to the electronic ground state  $X^3\Sigma_g^-$ . These fractions are independent of the initial condition, i.e. whether initially recombination into the  $X^3\Sigma_g^-$  or  $b^1\Sigma_g^+$  state occurs, which indicates that the simulations are converged.

Of all simulations, a fraction of 14% and 19% for the  $X^3\Sigma_g^-$  and  $b^1\Sigma_g^+$  states, respectively, does not lead to recombination and stabilization of O<sub>2</sub>. Instead, the two oxygen atoms remain separated on the surface, see Figure 3A. For a small number of trajectories (2% and 1%, respectively) a single collision leads to O<sub>2</sub> with subsequent scattering and dissociation back into two separated oxygen atoms. Finally, there is also a small number of trajectories (13 which initially recombine into  $X^3\Sigma_g^-$  and 12 that recombine into  $b^1\Sigma_g^+$ ) which have not settled into a final electronic state after 400 ps and exploration of the electronic manifold continues on longer time scales.

The two state model indicates that recombination of two <sup>3</sup>P oxygen atoms into O<sub>2</sub> in both electronic states is possible. Furthermore, vibrational relaxation and stabilization in these two states occurs on considerably longer time scales than a few hundred picoseconds, as was already found in previous work.<sup>24</sup> For a more comprehensive characterization, the third electronic state ( $a^1\Delta_g$ ), that also correlates with <sup>3</sup>P oxygen is also included in a next step.

## 2.2 Three state model

As a more realistic scenario, a three state model that includes the first three electronic states ( $X^3\Sigma_g^-$ ,  $a^1\Delta_g$  and  $b^1\Sigma_g^+$ ) is considered. The transition between the  $X^3\Sigma_g^-$ , and the  $b^1\Sigma_g^+$  state



is treated in the same way as for the 2-state model. For transitions between  $X^3\Sigma_g^-$  and  $a^1\Delta_g$  it is noted that the *ab initio* calculations show that the spin orbit coupling is different from zero only in the coupling region (see Figure S7) whereas no transitions between the  $a^1\Delta_g$  and  $b^1\Sigma_g^+$  states are considered because the two potential energy curves do not cross and SOC and NAC matrix elements are zero. Overall, the  $^3\Sigma_g^- \longleftrightarrow ^1\Delta_g$  and  $^3\Sigma_g^- \longleftrightarrow ^1\Sigma_g^+$  are included in this model.

For the three-state model 666 simulations were run. While  $O_2$  is in one of the two excited singlet states, the only possible transition leads to the ground state. This reflects the fact that the SOC and NAC matrix elements between the two excited states is zero. For a transition from the ground state to both excited states the more probable of the two is chosen. To determine which transition takes place,  $P_{LZ}^{j \rightarrow k}$  is evaluated for both transitions and compared with a random number ( $z$ ). If  $P_{LZ}^{j \rightarrow k} > z$  for both transitions, the one with the larger value of  $P_{LZ}^{j \rightarrow k}$  is chosen.

Transitions  $^3\Sigma_g^- \rightarrow a^1\Delta_g$  occur at smaller interatomic distances (2.09 Å, see Figure S1), compared to an average value of 2.21 Å for the  $^3\Sigma_g^- \rightarrow b^1\Sigma_g^+$  transition, see Figure S5B. Including the  $^3\Sigma_g^- \rightarrow a^1\Delta_g$  transition into the reaction model leads to an increase of  $\tau_{LZ}$  to  $326.8 \pm 226.2$  ps, see Figure 4. While the population on the highest  $b^1\Sigma_g^+$  state stabilizes after  $\sim 200$  ps, transitions between the  $X^3\Sigma_g^+$  and the  $a^1\Delta_g^+$  states continue out to  $\sim 700$  ps. Thus, the value of  $\tau_c$  represents an average over the total population distribution for the two states ( $^3\Sigma_g^- \rightarrow a^1\Delta_g$ , around 500 ps, and  $^3\Sigma_g^- \rightarrow b^1\Sigma_g^+$ , 100 ps). Including a third state with a crossing point at shorter O–O separation makes the transition time longer. As a consequence, transitions involving  $a^1\Delta_g$  are more prevalent than those involving  $b^1\Sigma_g^+$ . The  $X^3\Sigma_g^- \rightarrow a^1\Delta_g$  transition occurs with a probability of 76 % whereas the  $X^3\Sigma_g^- \rightarrow b^1\Sigma_g^+$  occurs for 24 % with fluctuations of 22 %.

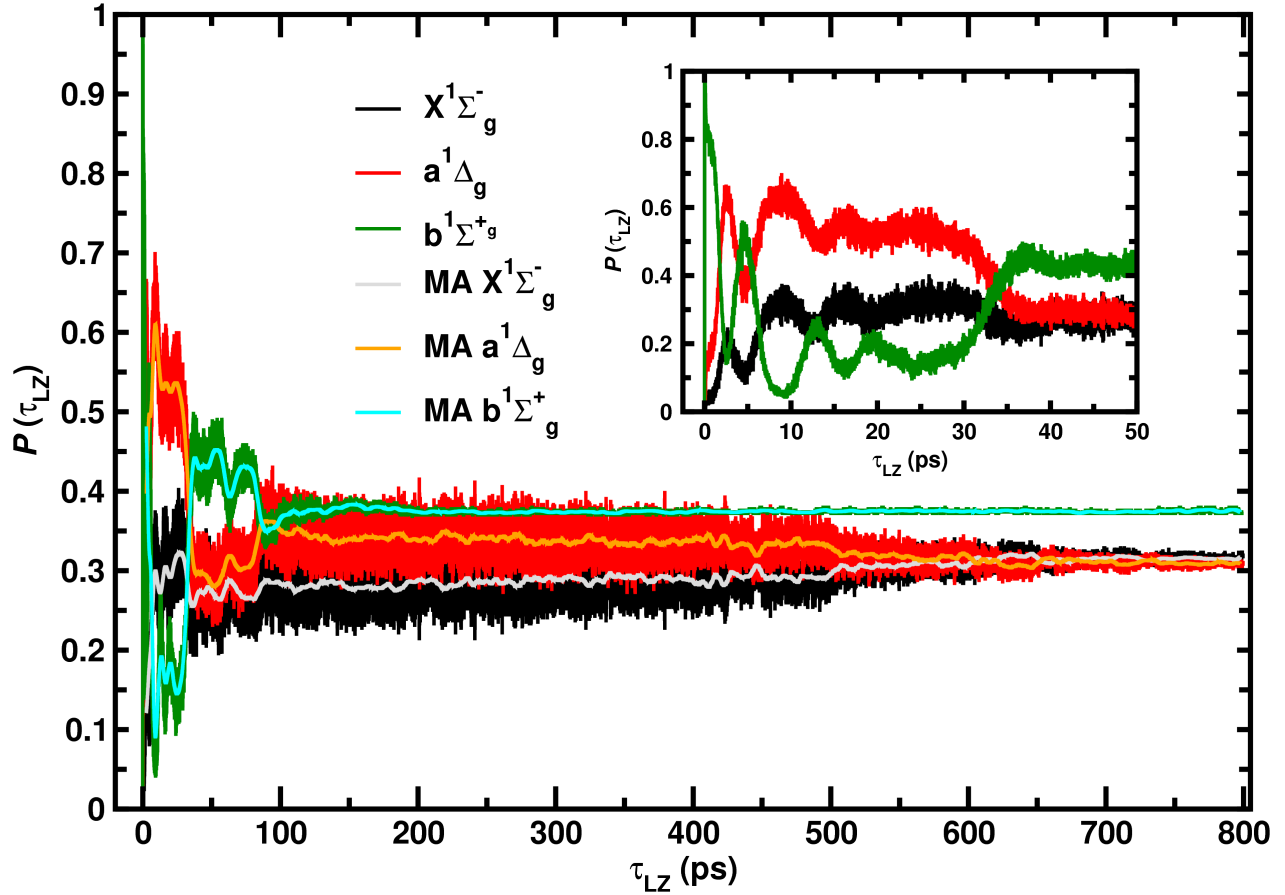


Figure 4: Population of the three electronic states and their moving average (MA) as a function of time (main panel) and a magnification of the first 50 ps in the inset. The zero along the  $x$ -axis is defined as the first transition in each of the 222 trajectories that initially rebind into  $b^1\Sigma_g^+$ . All the population will be initially on the  $b^1\Sigma_g^+$  state. As the dynamics proceeds, the population of the  $b^1\Sigma_g^+$  state stabilizes at  $\sim 38\%$  within  $\sim 200$  ps. The population dynamics for the  $X^3\Sigma_g^-$  and  $a^1\Delta_g$  states continues until  $> 500$  ps.

Figure 4 shows how the population of the three states differs after the first transition. After recombination on the ground state, the first transition leads to the  $b^1\Sigma_g^+$ , common for all simulations. The first 200 ps are characterized by exchange of population between the three state. After this time, population on  $b^1\Sigma_g^+$  reaches its equilibrium value. A slower exchange of population occurs between the two lower states ( $^3\Sigma_g^-$  and  $a^1\Delta_g$ ) for a longer period of time ( $\sim 500$  ps) before reaching the equilibrium population.

The final state distributions for the three-state model is summarized in Figure 3B. For the two-state model, population of the  $b^1\Sigma_g^+$  state is twice more probable than the ground state  $X^3\Sigma_g^-$ . For the three-state model, the  $b^1\Sigma_g^+$  state is still most probable, with the  $X^3\Sigma_g^-$  and  $a^1\Delta_g$  states equally probable. Probabilities for individual events are comparable with those found for the two states model: the final ground state population is  $\sim 25$  %, trajectories without collision of atomic oxygen occurs for  $< 20$  % and the population at the excited state assume values greater than 50 %.

A final question concerns the validity of classical MD simulations to follow the population dynamics between two or multiple states. For this, a wave packet with a translational energy of 2.1 kcal/mol was initialized on the  $X^3\Sigma_g^-$  PES and propagated with a time step of 0.125 fs allowing for transitions between the  $X^3\Sigma_g^-$  and  $b^1\Sigma_g^+$  states. The Fourier transformation of the initial wavefunction as a function of energy (see Figure S10) shows that an energy range of 0.03–5.0 kcal/mol is covered which is required to capture the low-energy part of the motion, characteristic for a surface temperature of 10 K to 50 K.

The time evolution of the wave function is shown in Figure 5 (black for  $X^3\Sigma_g^-$  and green for  $b^1\Sigma_g^+$ ). Initially ( $t = 0$ ,  $r = 8.0$  Å), the system is on the  $X^3\Sigma_g^-$  surface. The radial grid consists of 1250 evenly spaced points from 0.35 to 26.8 Å and the damping function starts at 15.0 Å. After  $\sim 250$  fs the wavepacket has passed the crossing region, splits into two parts,

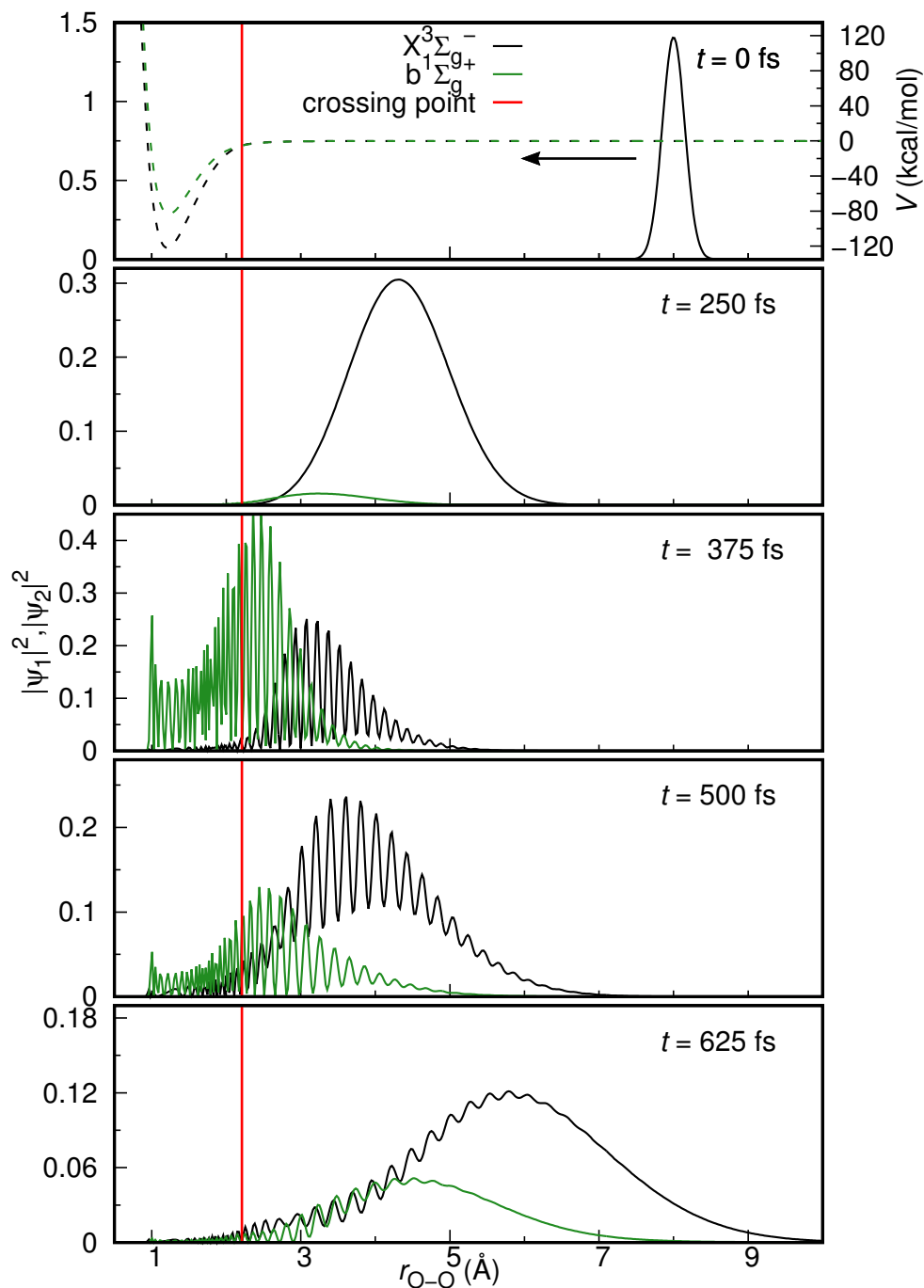


Figure 5: Probability distribution of the wave function  $|\Psi|^2$  (solid black and green lines) at different simulation times for both states. The potential energies along the diatomic separation are also plotted by dashed lines for the corresponding states. Crossing point is shown on 'X' axis as red lines.

and the amplitude on the  $b^1\Sigma_g^+$  PES starts to increase. The distribution of population as a function of time is shown in Figure S9. Significant amount of population transfers from the  $X^3\Sigma_g^-$  state to the  $b^1\Sigma_g^+$  state occurs up to 380 fs, although some amount of the WP transfers back to the  $X^3\Sigma_g^-$  state due to the coupling of the two states. Since the QM simulations are carried out in the gas phase, only one single collision can be followed. However, in the condensed phase, vibrational relaxation can form a bound  $O_2$  molecule. Multiple crossings are thus possible for the high lying vibrational states of  $O_2$  molecule.

To account for the recurrences, a kinetic model has been constructed for multiple crossings of the WP, see Figure S11. In gas phase the transition probabilities from one state to another starting from any of the states are equal. Hence, the kinetic model for 2 states leads to a stationary population of 50% on each of the  $X^3\Sigma_g^-$  and  $b^1\Sigma_g^+$  states. Here, it is worth mentioning that this ratio is 66 % on  $b^1\Sigma_g^+$  and 34 % on  $X^3\Sigma_g^-$  obtained from the condensed phase classical MD simulations. A possible explanation for this observation is the different coupling between the  $O_2$  motion and the surrounding water matrix due to the different curvatures of the potential energy curves for the two electronic states. A similar kinetic model for 3-state model leads to a stationary statistical population of 1/3 on each state, which is close to the classical MD simulations (31 %, 31 %, and 38 % for the  $X^3\Sigma_g^-$ ,  $a^1\Delta_g$  and  $b^1\Sigma_g^+$  states, respectively).

### 3 Conclusion

The present work establishes that upon recombination of  $^3P$  atomic oxygen on ASW, molecular oxygen ( $O_2$ ) in its ground and lower electronically excited states can be formed and stabilized. It should be emphasized that desorption of  $O_2$  after formation through association of atomic oxygen, although energetically feasible, was not observed. This is consistent

with earlier work.<sup>24</sup>

For singlet oxygen, the radiative decay lifetimes have been determined in the gas phase. They range from  $\sim 1$  min to  $\sim 100$  min for the  $a^1\Delta_g$  and  $b^1\Sigma_g$  states and also depend on the vibrational level.<sup>13,23</sup> Thus, the actual fraction available for chemical processes will depend on how the radiative lifetime changes when  $O_2$  is adsorbed on ASW. Because the reactivity of the  $a^1\Delta_g$  and  $b^1\Sigma_g^+$  states can be considerably larger than that of the  $X^3\Sigma_g^-$  ground state depending on the reaction partner, including electronically excited states of  $O_2$  (and other molecules formed on ASW) may be essential for a comprehensive modeling and understanding of the chemistry of interstellar matter under such conditions.

## Acknowledgments

This work was supported by the Swiss National Science Foundation through grants 200021-117810, and the NCCR MUST.

## References

- (1) Angell, C. A. 2004, *Annu. Rev. Phys. Chem.*, 55, 559
- (2) Bossa, J.-B., Maté, B., Fransen, C., et al. 2015, *Astrophys. J.*, 814, 47
- (3) Bossa, J.-B., Isokoski, K., Paardekooper, D. M., et al. 2014, *A&A*, 561, A136
- (4) Burke, D. J., & Brown, W. A. 2010, *Phys. Chem. Chem. Phys.*, 12, 5947
- (5) Cazaux, S., Bossa, J.-B., Linnartz, H., & Tielens, A. G. G. M. 2015, *A&A*, 573, A16
- (6) Chaabouni, H., Minissale, M., Manic, G., et al. 2012, *J. Chem. Phys.*, 137, 234706
- (7) Chou, S.-L., Lo, J.-I., Peng, Y.-C., et al. 2018, *Phys. Chem. Chem. Phys.*, 20, 7730

- (8) Chukalovsky, A. A., Klopovsky, K. S., Liberman, M. A., et al. 2012, *Combust. Sci. Technol*, 184, 1768
- (9) Chukalovsky, A. A., Klopovsky, K. S., Palov, A. P., Mankelevich, Y. A., & Rakhimova, T. V. 2016, *J. Phys. D*, 49, 485202
- (10) Dayou, F., Hernandez, M. I., Campos-Martinez, J., & Hernandez-Lamoneda, R. 2005, *J. Chem. Phys.*, 123, 074311
- (11) Dulieu, F., Minissale, M., & Bockelée-Morvan, D. 2017, *A&A*, 597, A56
- (12) Farooq, Z., Chestakov, D. A., Yan, B., et al. 2014, *Phys. Chem. Chem. Phys.*, 16, 3305
- (13) Gamache, R., Goldman, A., & Rothman, L. 1998, *J. Quant. Spectrosc. Radiat. Transf.*, 59, 495
- (14) Hama, T., & Watanabe, N. 2013, *Chem. Rev.*, 113, 8783
- (15) Hidemori, T., Akai, N., Kawai, A., & Shibuya, K. 2012, *J. Phys. Chem. A*, 116, 2032
- (16) Ioppolo, S., Cuppen, H. M., & Linnartz, H. 2011, *Rend. Lincei.-Sci. Fis. Nat*, 22, 211
- (17) Jongma, R. T., Shi, S., & Wodtke, A. M. 1999, *J. Chem. Phys.*, 111, 2588
- (18) Lakshmanan, S., Pratihari, S., & Hase, W. L. 2019, *J. Phys. Chem. A*, 123, 4360
- (19) Minaev, B. F., & Yashchuk, L. B. 2003, *Opt. Spectrosc*, 95, 553
- (20) Minissale, M., Fedoseev, G., Congiu, E., et al. 2014, *Phys. Chem. Chem. Phys.*, 16, 8257
- (21) Minissale, M., Moudens, A., Baouche, S., Chaabouni, H., & Dulieu, F. 2016, *Mon. Not. Roy. Astron. Soc.*, 458, 2953
- (22) Minissale, M., Nguyen, T., & Dulieu, F. 2019, *Astron. Astrophys.*, 622, A148

- (23) Newman, S., Lane, I., Orr-Ewing, A., Newnham, D., & Ballard, J. 1999, *J. Chem. Phys.*, 110, 10749
- (24) Pezzella, M., & Meuwly, M. 2019, *Phys. Chem. Chem. Phys.*, 21, 6247
- (25) Pezzella, M., Unke, O. T., & Meuwly, M. 2018, *J. Phys. Chem. Lett.*, 9, 1822
- (26) Romanzin, C., Ioppolo, S., Cuppen, H. M., van Dishoeck, E. F., & Linnartz, H. 2011, *J. Chem. Phys.*, 134, 084504
- (27) Song, X., Fanelli, M. G., Cook, J. M., Bai, F., & Parish, C. A. 2012, *J. Phys. Chem. A*, 116, 4934
- (28) Starik, A. M., Loukhovitski, B. I., Sharipov, A. S., & Titova, N. S. 2015, *Philos. Trans. Royal Soc. A*, 373, 20140341
- (29) T. Nagy, J. Y. R., & Meuwly, M. 2014, *J. Chem. Theo. Comp.*, 10, 1366



# Supplementary Information: Formation and Stabilization of Ground and Excited State Singlet $O_2$ upon Recombination of $^3P$ Oxygen on Amorphous Solid Water

Marco Pezzella, Debasish Koner and Markus Meuwly\*

*Department of Chemistry, University of Basel, Klingelbergstrasse 80, CH-4056 Basel, Switzerland.*

E-mail: m.meuwly@unibas.ch

## Methods

The simulation system consists of an equilibrated cubic box of amorphous solid water with dimension  $31 \times 31 \times 31 \text{ \AA}^3$  containing 1000 TIP3P<sup>1</sup> water molecules, and two oxygen atoms, see Figure 1. The time step in all simulations was  $\Delta t = 0.1 \text{ fs}$  which ensures conservation of total energy also during the recombination dynamics. All bonds involving hydrogen atoms were constrained using SHAKE<sup>2</sup> and the non-bonded cutoff was at  $13 \text{ \AA}$ . Initial conditions were generated from an existing, equilibrated ASW structure<sup>3,4</sup> by adding two oxygen atoms, minimizing the system, heating it for 5 ps to 50 K and equilibrating for 10 ps. Data (energies, coordinates and velocities) are saved every 1,000 steps. This was followed by production simulations of various lengths, as indicated throughout this work.

All simulations are performed using the CHARMM program<sup>5</sup> modified for reactive MD simulations<sup>6,7</sup> and potential energy surfaces for O<sub>2</sub> based on reproducing kernels.<sup>8,9</sup> For treating nonadiabatic transitions a surface hopping scheme based on the Landau Zener formalism is used, see below. Three electronic states for O<sub>2</sub> are considered: the ground state ( $X^3\Sigma_g^-$ ) and the next two electronically excited states ( $a^1\Delta_g$  and  $b^1\Sigma_g^+$ ) based on earlier calculations at the MRCI/aug-cc-pVTZ level of theory<sup>10</sup> which were accurately represented as a reproducing kernel Hilbert space (see Figure S1a).<sup>8,9</sup> The spin orbit coupling (SOC) matrix elements involving the  $^3\Sigma_g^-$  and  $^1\Sigma_g^+$  states were recomputed at the MRCI/aug-cc-pVTZ level of theory and can be compared with previous works at the CI/cc-pVTZ<sup>11</sup> and CASSCF/CASPT2/5s4p3d2f atomic natural orbital basis set<sup>12</sup> levels of theory, see Figure S1b. Because the  $a^1\Delta_g$  and the  $b^1\Sigma_g^+$  states do not cross (see inset Figure S1) and the nonadiabatic coupling (NAC) matrix element between the two states is zero, transitions between these two states will not be included.

In the gas phase all transitions between the  $^3\Sigma_g^-$ ,  $^1\Delta_g$  and  $^1\Sigma_g^+$  states are strictly forbidden. Transitions from the ground state to the two excited states are spin-forbidden<sup>13</sup> and Laporte rule,<sup>14</sup> because all states have  $g$  symmetry. Due to the second rule, transitions between  $a^1\Delta_g$  and  $b^1\Sigma_g^+$  are also forbidden. However, because the reaction occurs on the ASW surface, no symmetry rules apply for allowed transitions. This is similar to the fact that  $Q$ -branches for diatomics in liquids and high pressure fluids become allowed due to symmetry breaking induced by the environment,<sup>15</sup> whereas such  $\Delta J = 0$  transitions are forbidden in free space.<sup>16</sup>

For the nonadiabatic transitions the trajectory surface hopping (TSH) method<sup>17</sup> within the Landau-Zener (LZ)<sup>18,19</sup> formalism was used. The implementation follows earlier work<sup>20,21</sup> for which the transition probability  $P_{LZ}^{i \rightarrow j}$  from state  $j$  to  $k$  is

$$P_{LZ}^{j \rightarrow k} = \exp \left( -2\pi \frac{(\Delta H_{jk})^2}{\hbar |\dot{\vec{R}} \cdot \vec{\nabla}(\Delta E_{jk})|} \right) \quad (S1)$$

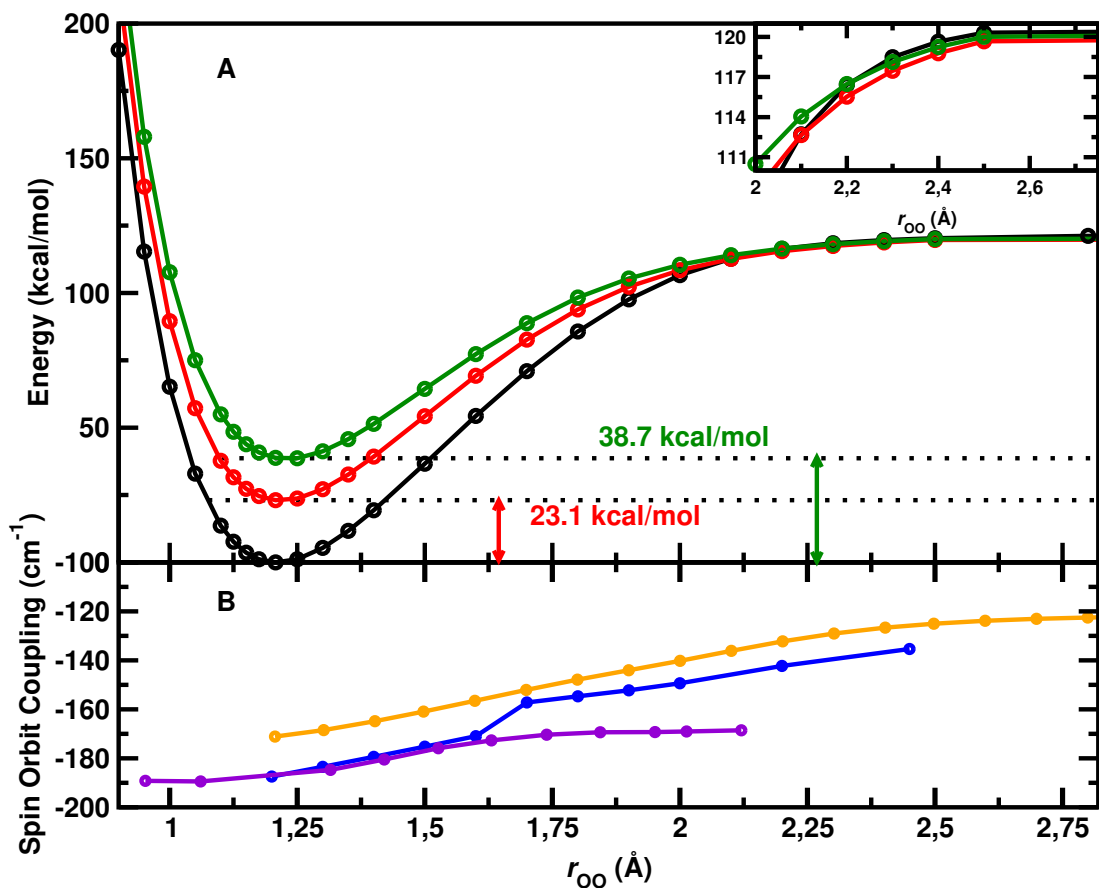


Figure S1: Panel A: Potential energy curves for the  $X^3\Sigma_g^-$ ,  $a^1\Delta_g$  and the  $b^1\Sigma_g^+$  states (black, red and green, respectively) with the crossing region enlarged in the inset. Panel B: SOC between the  $^3\Sigma_g^-$  and  $^1\Sigma_g^+$  states from the literature (blue<sup>11</sup> and violet<sup>12</sup>) and the SOC calculated in the present work (orange). The differences can be explained by the difference in methodologies and basis set between used in the different calculations. Asymptotically, the SOC approaches twice the value of O  $^3P$ , which is 74.182  $\text{cm}^{-1}$  for a single oxygen atom in its ground state.

The transition probability depends on the gradient of the energy difference  $\vec{\nabla}(\Delta E_{jk})$  between states  $j$  and  $k$ , the coupling  $\Delta H_{jk}$ , which is the conformationally dependent spin orbit matrix element, and the velocity of the center of mass  $\dot{\vec{R}}$  at the transition.

The trajectories are started from a given initial electronic state  $j$  and the electronic state is followed along the trajectory. Close to a crossing between the present state  $j$  and a neighboring state  $k$ ,  $P_{LZ}^{j \rightarrow k}$  is calculated and compared with a random number  $\xi \in [0, 1]$ . If  $P_{LZ}^{j \rightarrow k} \geq \xi$  a transition from state  $j$  to state  $k$  occurs. To ensure conservation of the total energy and total angular momentum, a momentum correction

$$\mathbf{p}' = \mathbf{p} - \hat{\mathbf{n}} \frac{\hat{\mathbf{n}} \mathbf{M}^{-1} \mathbf{p}}{\hat{\mathbf{n}} \mathbf{M}^{-1} \hat{\mathbf{n}}} \left[ 1 - \left( 1 - 2\Delta E \frac{\hat{\mathbf{n}} \mathbf{M}^{-1} \hat{\mathbf{n}}}{(\hat{\mathbf{n}} \mathbf{M}^{-1} \mathbf{p})^2} \right)^{1/2} \right], \quad (\text{S2})$$

is applied<sup>22</sup> where  $\mathbf{p}$  and  $\mathbf{p}'$  are the momenta before and after the hop and  $\mathbf{M}$  is the mass matrix and  $\hat{\mathbf{n}}$  is the unit vector along the velocity direction.

In order to assess the role of quantum effects on the nuclear dynamics, time-dependent wave packet (WP) simulations were carried out for the two state model (see below), including the  $X^3\Sigma_g^-$  and  $b^1\Sigma_g^+$  states. For this, the time-dependent Schrödinger equation is<sup>23-25</sup>

$$\begin{pmatrix} \psi_1(r; t) \\ \psi_2(r; t) \end{pmatrix} = e^{-iHt/\hbar} \begin{pmatrix} \psi_1(r; 0) \\ \psi_2(r; 0) \end{pmatrix} \quad (\text{S3})$$

where the Hamiltonian  $H$  is

$$\hat{H} = -\frac{\hbar^2}{2\mu} \frac{\partial^2}{\partial r^2} + \begin{pmatrix} V_{11}(r) & V_{12}(r) \\ V_{21}(r) & V_{22}(r) \end{pmatrix} \quad (\text{S4})$$

where  $\mu$  is the reduced mass of the system,  $V_{11}$ ,  $V_{22}$  are the diabatic potential energies and  $V_{12} = V_{21}$  is the geometry-dependent coupling matrix element between two states.

The initial wave packet is a (complex-valued) Gaussian function

$$\psi_0(r) = (1/2\pi\sigma^2)^{1/4} \exp[-1/(2\sigma^2)(r - r_0)^2] \exp[ip_0(r - r_0)], \quad (\text{S5})$$

where  $\sigma$  is the width parameter,  $r_0$  and  $p_0$  are the initial position and momentum of the wavepacket, respectively. The time-dependent wave function is propagated<sup>26</sup> on the coupled  $X^3\Sigma_g^+$  and  $b^1\Sigma_g^+$  potentials using the split-operator method.<sup>27</sup> Fast Fourier transformation (FFT) is used to calculate the double differentiation  $\frac{\partial^2}{\partial r^2}$  of the wave function. A sine damping function is multiplied to the wave function at the grid boundary to avoid reflection. The state population can then be calculated as the expectation value of the projection operator<sup>25</sup>

$$P_2(t) = \left\langle \begin{pmatrix} \psi_1(x; t) \\ \psi_2(x; t) \end{pmatrix} \middle| \begin{pmatrix} 0 & 0 \\ 0 & 1 \end{pmatrix} \middle| \begin{pmatrix} \psi_1(x; t) \\ \psi_2(x; t) \end{pmatrix} \right\rangle \quad (\text{S6})$$

and  $P_1(t) = 1 - P_2(t)$ .

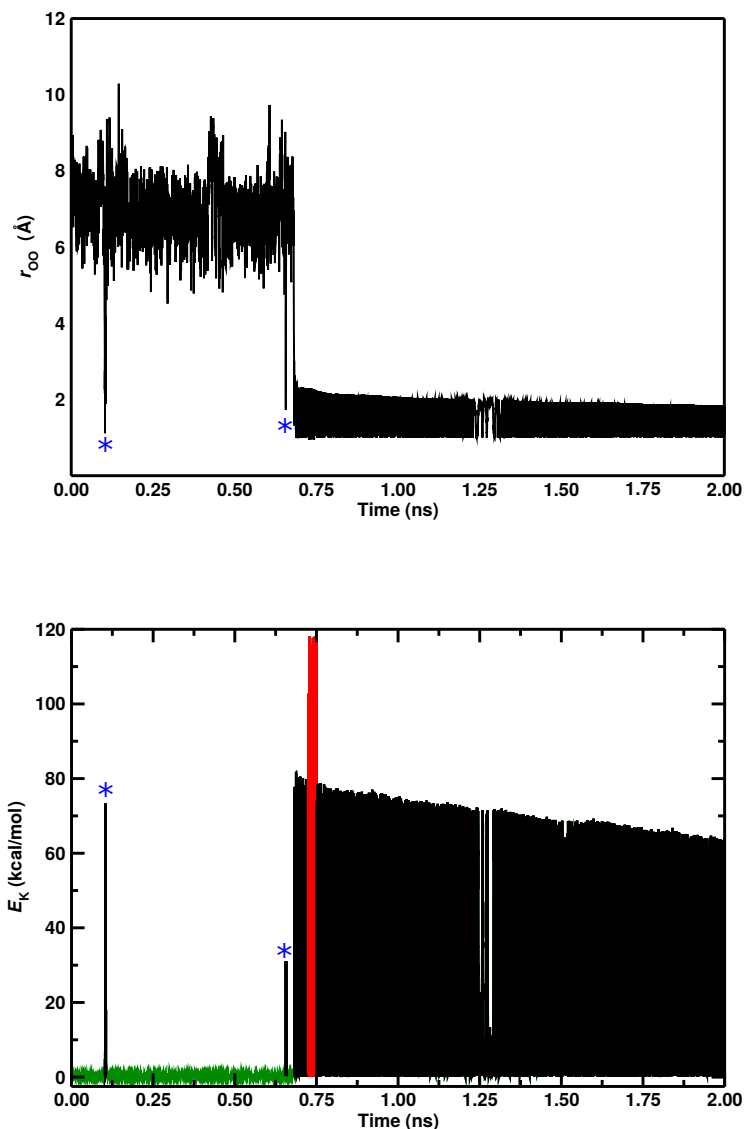


Figure S2: Top panel: time evolution of the interatomic distance between two oxygen atoms for the simulation inside the cavity. The first time that the bound state is reached, at 103.5 ps, it suddenly dissociates due the collision of the molecule with one of the TIP3P hydrogen water. A similar situation happens near the formation time (around 670 ps). Both are shown in the graph by a blue star. Bottom panel: kinetic energy for the dioxygen system. The bound state can be recognized by the peak in kinetic energy at 103.5 ps and at 670 ps (shown with a blue star). The transition between  $^1\Sigma_g^+$  and  $^3\Sigma_g^+$  is observed between 720 ps and 750 ps and is characterized by the  $\sim 40$  kcal/mol energy increase. This energy corresponds to the energy difference between the two states. A color code here is applied in order to distinguish the three different states: the green line represents the unbound state, the red one the time interval where the triplet region is explored and the black is used when  $O_2$  lays in the singlet state.

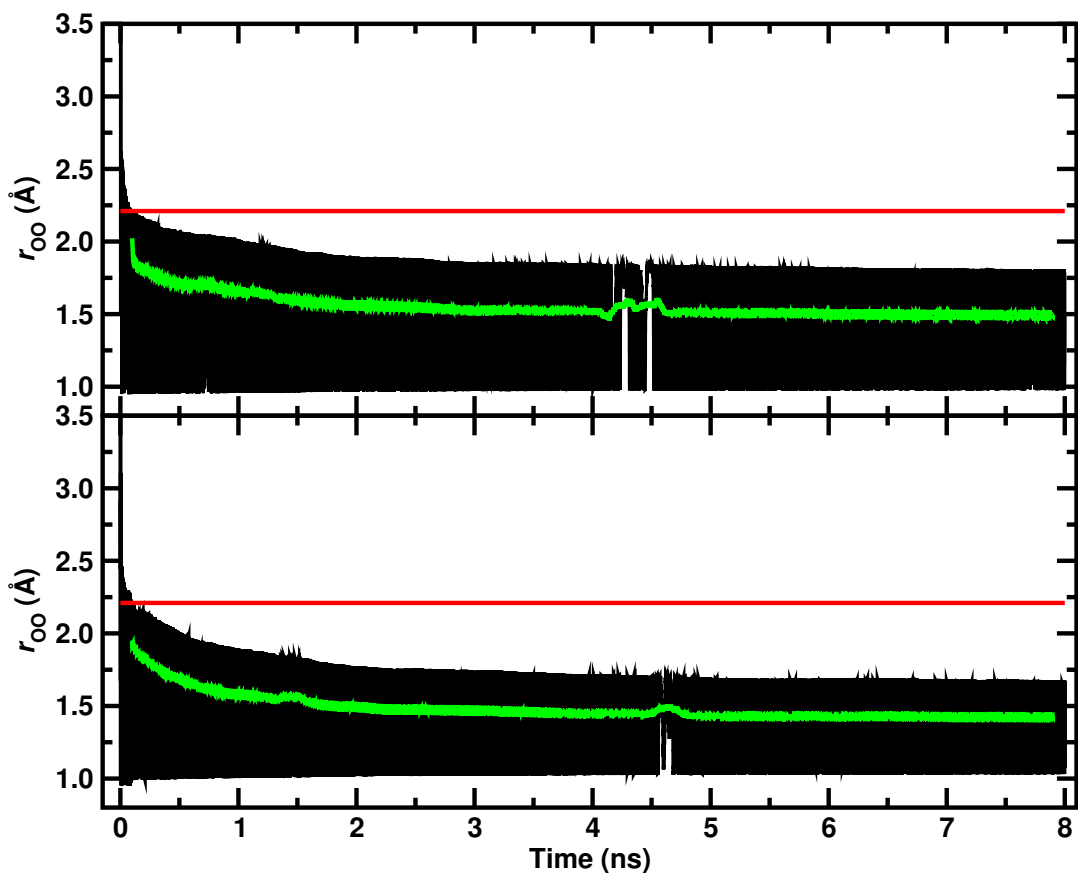


Figure S3: Relaxation of the O<sub>2</sub> bond length during two independent 8 ns simulation with the two states models for two simulations. Transitions are observed only in the initial steps of the simulations corresponding to the overlap between the time series and the crossing point between the two states (2.209 Å, red line). The green line represents the moving average of the time series over 0.2 ps time interval. The signatures between 4 ns and 4.5 ns are collisional re-excitation of the diatomic due to collisions with the surface.

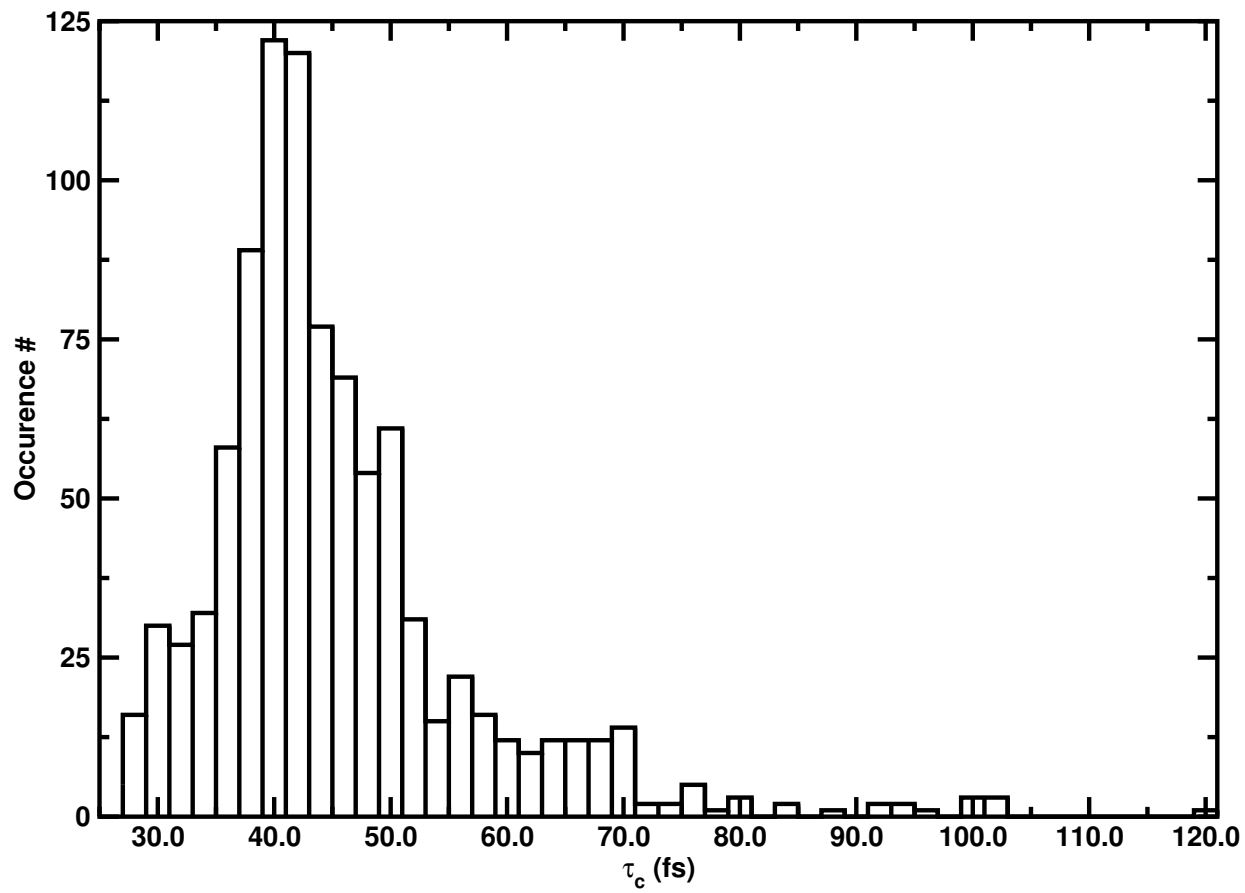


Figure S4: Probability distribution for  $\tau_c$ . The average is  $47.4 \pm 11.7$  fs. This corresponds to approximately one transition every two vibrational periods.



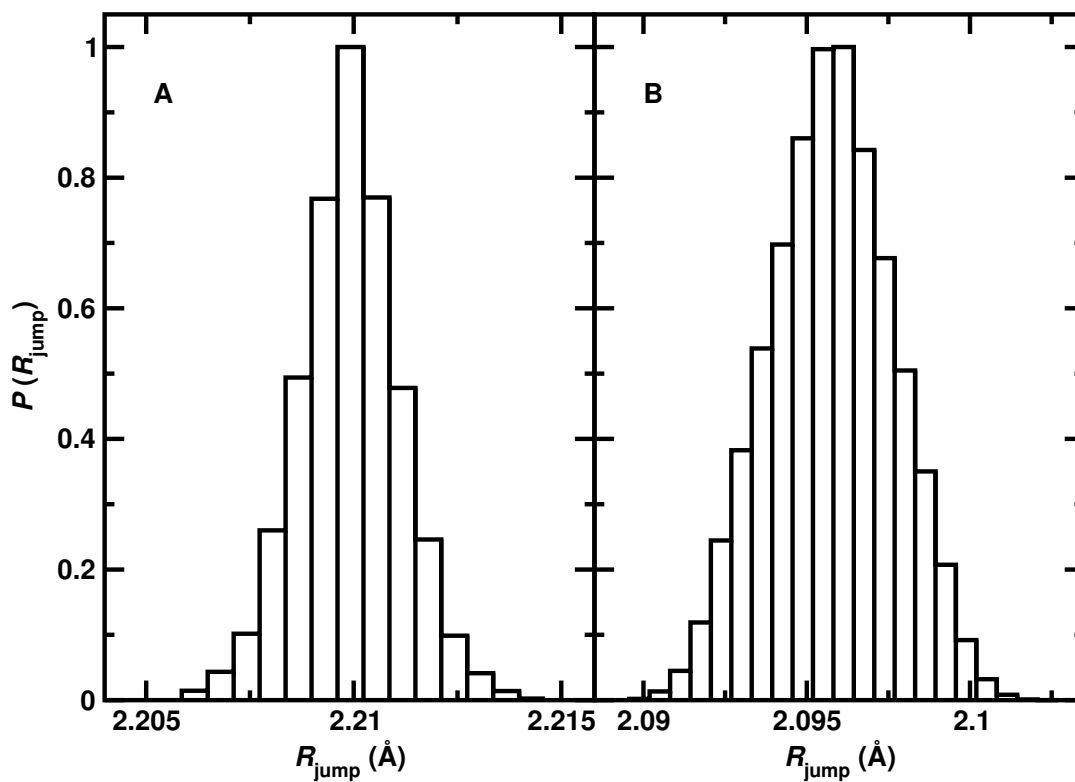


Figure S5: Probability distributions of the interatomic distance within the transition between the  $a^1\Delta_g^-$  and the  $X^3\Sigma_g^-$  (B),  $b^3\Sigma_g^-$  and the  $X^3\Sigma_g^-$  (A) for an ensemble of simulations.. In the first case the interval is localized around  $2.097 \pm 0.003 \text{ \AA}$  and in the second case around  $2.209 \pm 0.003 \text{ \AA}$ .

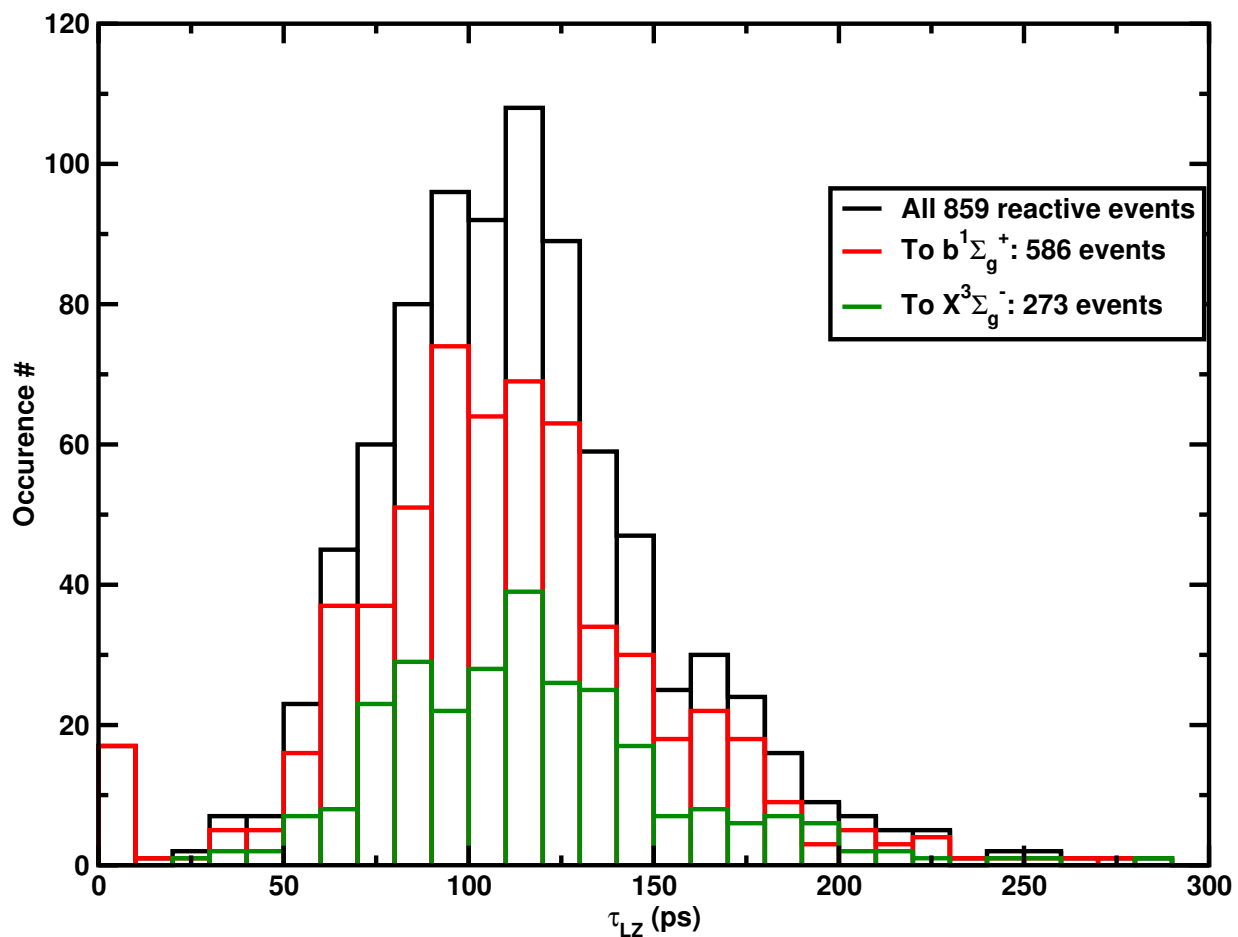


Figure S6: The time distribution for the three  $\tau_{LZ}$  for the  $O_2$  recombination from  $b^3\Sigma_g^-$ , in red simulations that from the initial  $X^3\Sigma_g^-$  state leads to final  $b^1\Sigma_g^+$  state, in green simulations that have  $X^3\Sigma_g^-$  as initial and final state The and in black the sum of the two previous sets.

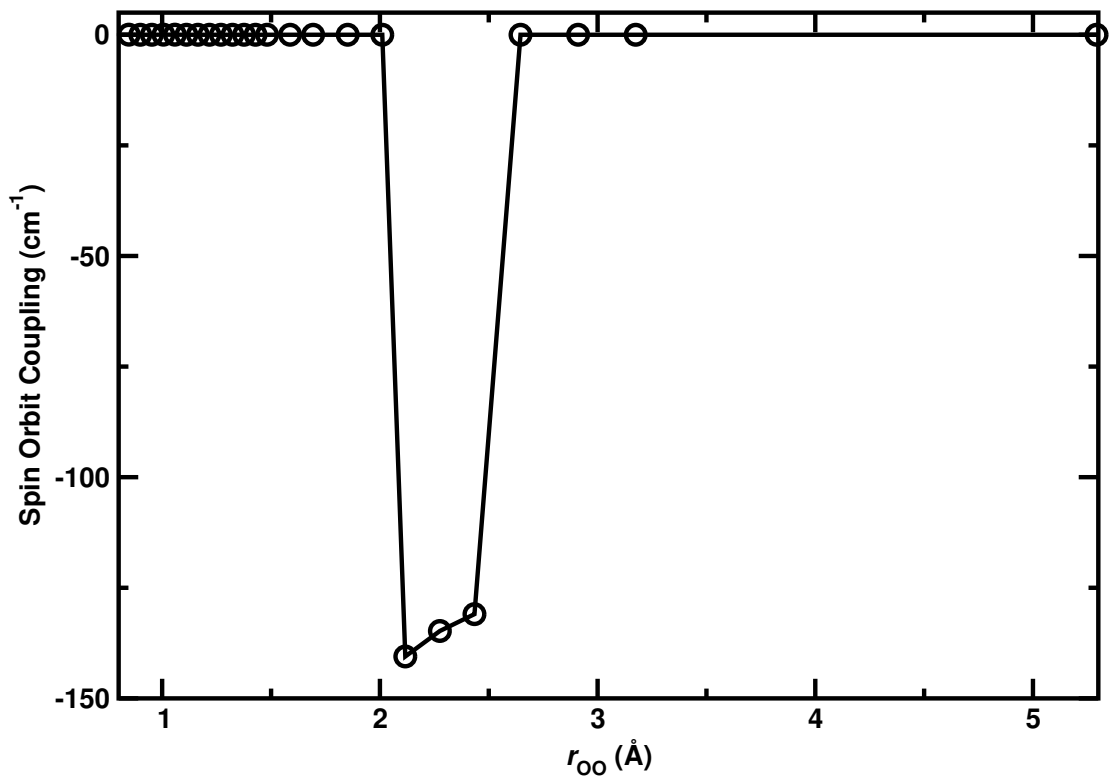


Figure S7: Computed spin orbit coupling between  $X^3\Sigma_g^-$  and  $a^1\Delta_g$ . The function is discontinuous, with values different from 0, only in the crossing regions. The two atoms are in the  $^3P$  state.

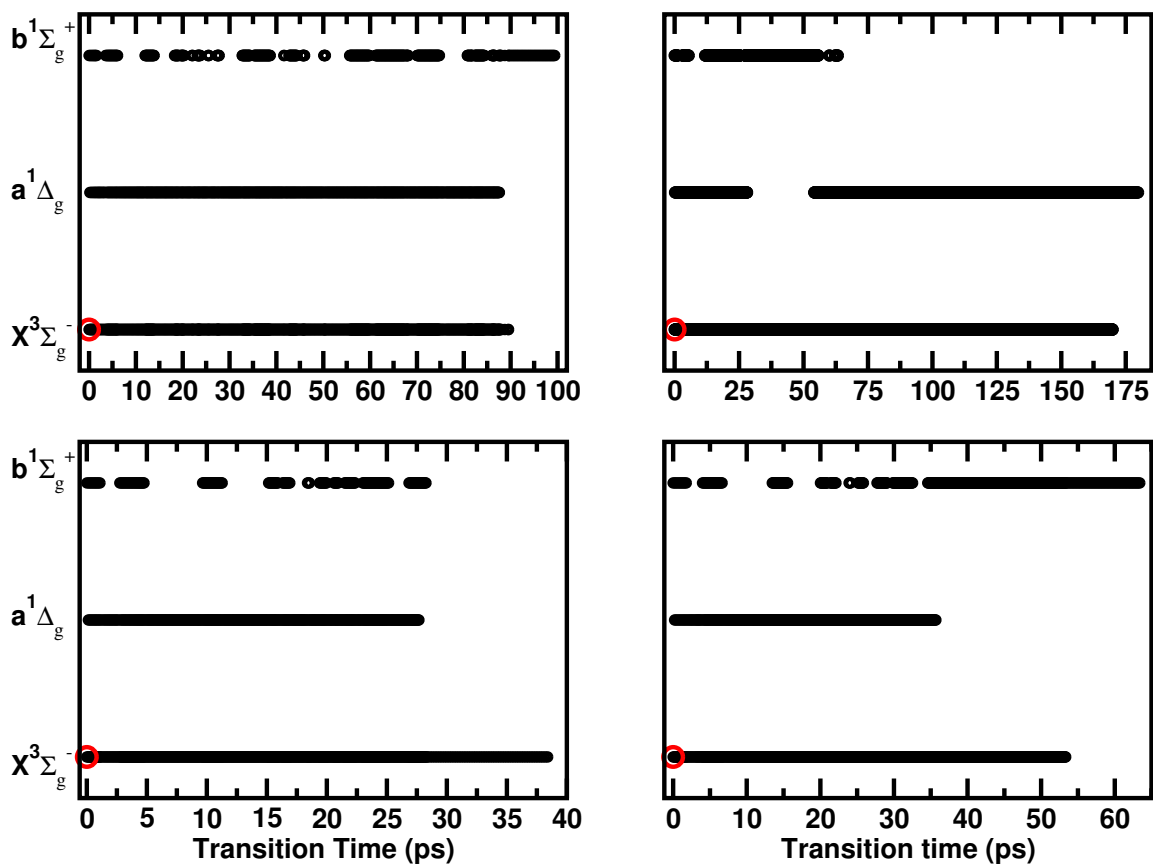


Figure S8: State dynamics for four different simulations during the  $\tau_{LZ}$  interval. All simulations start from the  $X^3\Sigma_g^-$  state (red dot).

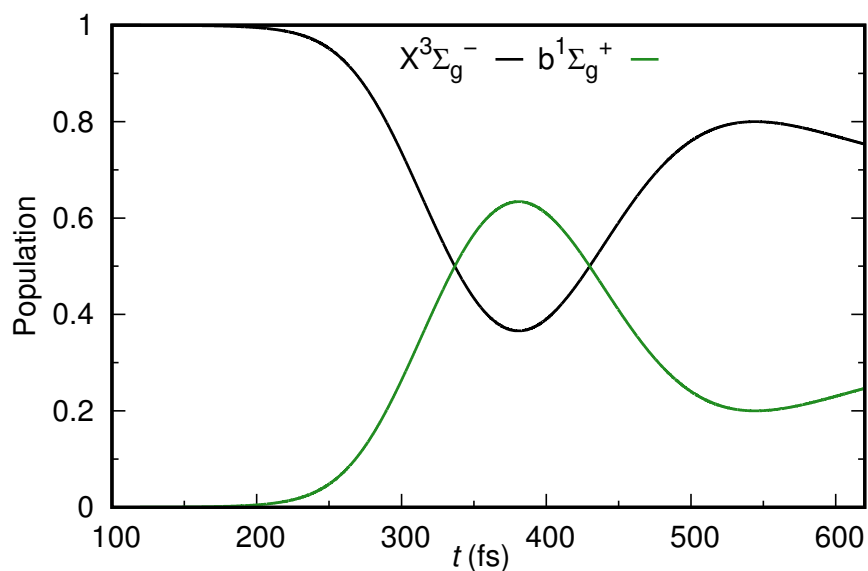


Figure S9: Population on each state as a function of time.

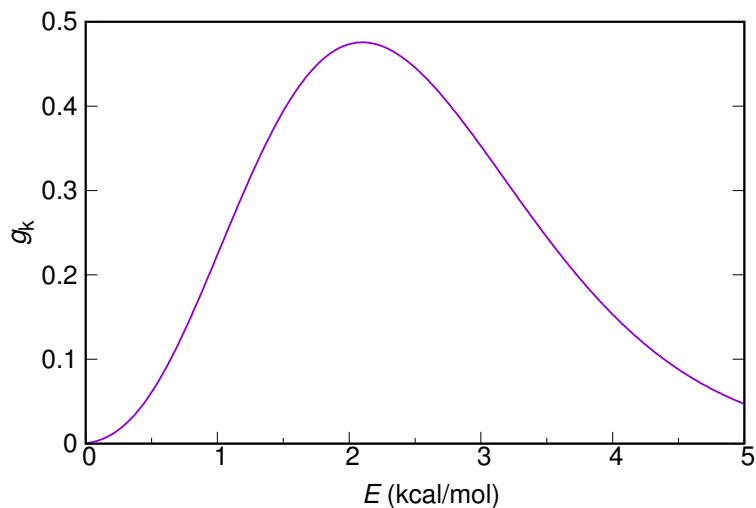


Figure S10: Fourier transform of the initial wave packet on  $X^3\Sigma_g^-$  state as a function of energy. The initial wave packet is a Gaussian function defined in Eq. 5 and  $g(k) = \frac{\sqrt{2\sigma}}{(2\pi)^{1/4}} \exp[-\sigma^2(k - p_0)^2] \exp(ir_0k)$ . where,  $k = \sqrt{2\mu E}$  and  $p_0 = \sqrt{2\mu E_0}$ .

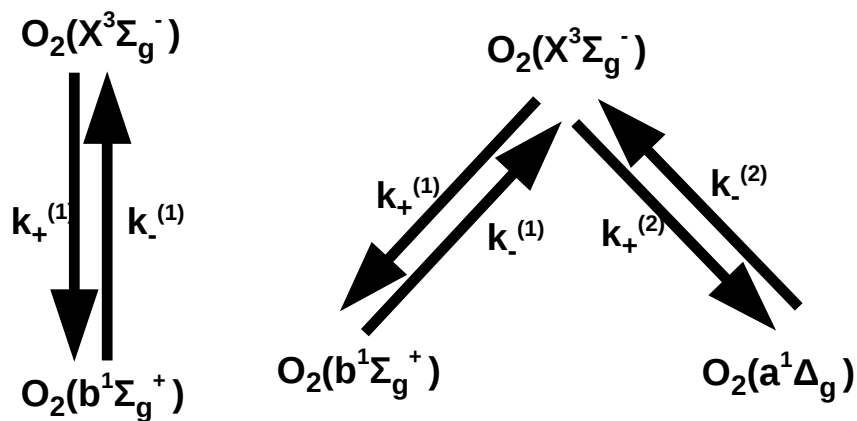


Figure S11: Kinetic model for multiple crossing. Left: 2-state model, right: 3-state model. Here,  $k$ s are the probabilities for the transition from one state to another.

## References

- (1) Jorgensen, W. L.; Chandrasekhar, J.; Madura, J. D.; Impey, R. W.; Klein, M. L. Comparison of simple potential functions for simulating liquid water. *J. Chem. Phys.* **1983**, *79*, 926–935.
- (2) van Gunsteren, W.; Berendsen, H. Algorithms for Macromolecular Dynamics and Constraint Dynamics. *Mol. Phys.* **1977**, *34*, 1311–1327.
- (3) Pezzella, M.; Unke, O. T.; Meuwly, M. Molecular Oxygen Formation in Interstellar Ices Does Not Require Tunneling. *J. Phys. Chem. Lett.* **2018**, *9*, 1822–1826.
- (4) Pezzella, M.; Meuwly, M. O<sub>2</sub> formation in cold environments. *Phys. Chem. Chem. Phys.* **2019**, *21*, 6247–6255.
- (5) Brooks, B. et al. CHARMM: the biomolecular simulation program. *J. Comp. Chem.* **2009**, *30*, 1545–614.
- (6) Meuwly, M. Reactive molecular dynamics: From small molecules to proteins. *Wiley Interdiscip. Rev.-Comput. Mol. Sci.* **2019**, *9*, e1386.
- (7) T. Nagy, J. Y. R.; Meuwly, M. Multi-Surface Adiabatic Reactive Molecular Dynamics. *J. Chem. Theo. Comp.* **2014**, *10*, 1366–1375.
- (8) Hollebeek, T.; Ho, T.-S.; Rabitz, H. Constructing Multidimensional Molecular Potential Energy Surfaces from ab Initio Data. *Ann. Rev. Phys. Chem.* **1999**, *50*, 537–570.
- (9) Unke, O. T.; Meuwly, M. Toolkit for the Construction of Reproducing Kernel-Based Representations of Data: Application to Multidimensional Potential Energy Surfaces. *J. Chem. Inf. Model.* **2017**, *57*, 1923–1931.
- (10) Bytautas, L.; Matsunaga, N.; Ruedenberg, K. Accurate ab initio potential energy curve of O<sub>2</sub>. II. Core-valence correlations and relativistic contributions and vibration-rotation spectrum. *J. Chem. Phys.* **2010**, *132*, 1–15.

- (11) Minaev, B. F.; Yashchuk, L. B. Spin-orbit coupling in oxygen near the dissociation limit. *Opt. Spectrosc* **2003**, *95*, 553–559.
- (12) Dayou, F.; Hernandez, M. I.; Campos-Martinez, J.; Hernandez-Lamonedá, R. Spin-orbit coupling in  $O_2(\nu)+O_2$  collisions: I. Electronic structure calculations on dimer states involving the  $X^3\Sigma_g^-$ ,  $a^1\Delta_g^+$ , and  $b^1\Sigma_g^+$  states of  $O_2$ . *J. Chem. Phys.* **2005**, *123*, 074311.
- (13) Herzberg, G.; Huber, K.-P. *Molecular Spectra and molecular structures*; Van Nostrand, 1950.
- (14) Laporte, O.; Meggers, W. F. Some Rules of Spectral Structure\*. *J. Opt. Soc. Am.* **1925**, *11*, 459–463.
- (15) Turrell, G. C.; Vu, H.; Vodar, B. Induced Q Branch in the Vibration-Rotation Spectrum of HCl Pressurized with Ar. *J. Chem. Phys.* **1960**, *33*, 315–316.
- (16) Herzberg, G. *Infrared and Raman Spectroscopy of Polyatomic Molecules*; Van Nostrand, 1954.
- (17) Stine, J. R.; Muckerman, J. T. On the multidimensional surface intersection problem and classical trajectory surface hopping. *J. Chem. Phys.* **1976**, *65*, 3975–3984.
- (18) Landau, L. D. Assotsiatsiya dvukhatomnykh molekul. *Phys. Z* **1932**, *2*, 46–52.
- (19) Zener, C. Non-adiabatic crossing of energy levels. *Proc. R. Soc. London A* **1932**, *137*, 696–702.
- (20) Belyaev, A. K.; Lebedev, O. V. Nonadiabatic nuclear dynamics of atomic collisions based on branching classical trajectories. *Phys. Rev. A* **2011**, *84*, 014701.
- (21) Belyaev, A. K.; Lasser, C.; Trigila, G. Landau–Zener type surface hopping algorithms. *J. Chem. Phys.* **2014**, *140*, 224108.

- (22) Miller, W. H.; George, T. F. Semiclassical Theory of Electronic Transitions in Low Energy Atomic and Molecular Collisions Involving Several Nuclear Degrees of Freedom. *J. Chem. Phys.* **1972**, *56*, 5637–5652.
- (23) Prudente, F. V.; Riganelli, A.; Marques, J. M. C. Time dependent wave packet study of the electronically non-adiabatic Cl + H<sub>2</sub> reaction using a one-dimensional model. *Phys. Chem. Chem. Phys.* **2003**, *5*, 2354–2359.
- (24) Mahapatra, S.; Köppel, H.; Cederbaum, L. S. Reactive Scattering Dynamics on Conically Intersecting Potential Energy Surfaces: The H + H<sub>2</sub> Exchange Reaction. *J. Phys. Chem. A* **2001**, *105*, 2321–2329.
- (25) Köppel, H.; Domcke, W.; Cederbaum, L. S. *Advances in Chemical Physics*; 2007; pp 59–246.
- (26) Koner, D.; Panda, A. N. Quantum Dynamical Study of the He + NeH<sup>+</sup> Reaction on a New Analytical Potential Energy Surface. *J. Phys. Chem. A* **2013**, *117*, 13070–13078.
- (27) Feit, M. D.; J. A. Fleck, J.; Steiger, A. Solution of the Schrödinger Equation by a Spectral Method. *J. Comp. Phys.* **1982**, *47*, 412 – 433.